

The Interstellar Environment of Filled-Center Supernova Remnants: II. G63.7+1.1

B.J. Wallace

T.L. Landecker

Dominion Radio Astrophysical Observatory

and

A.R. Taylor

The Department of Physics and Astronomy, The University of Calgary

ABSTRACT

A multi-wavelength investigation of the candidate supernova remnant G63.7+1.1 and its surrounding interstellar medium is presented. On the basis of radio continuum data we conclude that the object is a filled-center supernova remnant, perhaps in the course of becoming a composite remnant. The morphology of the remnant, along with HI, ^{12}CO and high resolution IRAS data, suggest that G63.7+1.1 is interacting directly with the ISM, and does not lie in a low density region of the ISM. This in turn strongly suggests that the detected nebula is not surrounded by an invisible halo of supernova ejecta. The association between the SNR and HI and CO features near the tangent point implies a kinematic distance for G63.7+1.1 of 3.8 ± 1.5 kpc.

Subject headings: supernova remnants — ISM: individual (G63.7+1.1) — radio continuum: ISM — radio lines: ISM — infrared: ISM: continuum

1. Introduction

Of the 215 Galactic supernova remnants (SNRs) cataloged by Green (1996), only 9 have been classified as filled-center (FC, also known as “Crab-like” or “plerionic”). An object classified as a FC SNR must have a centrally brightened radio morphology, a flat ($\alpha > -0.3$), non-thermal, radio spectral index, and a complete lack of an associated limb-brightened shell. It is assumed that the radio emission from these objects is powered by a pulsar interior to the nebula, even if no pulsar has been detected. An object which is

centrally brightened but has an associated limb-brightened shell is classified as a composite remnant.

The distinction between FC and composite SNRs highlights an important problem associated with FC SNRs, the absence of the limb-brightened shell. If both these types of objects are formed by supernovae which produce pulsars, why should one type have an associated shell but not the other? The most appealing theory to explain the lack of a shell around FC SNRs is that put forward by Chevalier (1977) who proposed that the Crab Nebula (and by extension other FC SNRs) consists of two components, a central pulsar-powered core, which makes up the detected component of the SNR, and an invisible halo of ejecta, formed at the same time as the central pulsar, moving at $\sim 10^4$ km/s. He surmised that the fast-moving ejecta around these objects are invisible because the FC SNRs lie in low density regions of the ISM and the surrounding halos of ejecta have interacted with only minimal amounts of material; presumably composite SNRs then lie in more “normal” environments and the shell is a direct result.

This hypothesis can be tested by directly imaging the interstellar medium (ISM) around FC SNRs to determine whether they lie in low density environments. Romani et al. (1990) used archival IRAS and HI data and concluded that the Crab Nebula lies in a large-scale, low-density void in the ISM. Similarly, Wallace et al. (1994) observed the Crab, 3C58, G74.9+1.2 and G21.5-0.9, and found evidence that all but G21.5-0.9 lie in voids (the data for G21.5-0.9 were inconclusive). These studies were limited by their poor resolution ($\sim 36'$) however, and higher resolution studies are required to image the ISM distribution immediately around these, and similar, objects.

This paper is the second of a series in which the ISM around FC SNRs is imaged at high resolution. The first paper (Wallace et al. 1997) came to the surprising conclusion that G74.9+1.2 does *not* lie in a low density region of the ISM (despite a low density region being suggested by the observations presented in Wallace et al. 1994). In this paper we present the results of a multi-frequency investigation into the FC SNR candidate G63.7+1.1 and its surroundings. G63.7+1.1 was identified as a FC SNR candidate by Taylor et al. (1992) based upon its non-thermal radio spectrum, low ratio of infrared to radio flux density, and morphology (the entire survey on which Taylor et al. (1992) is based can be found in Taylor et al. 1996). The data of Taylor et al. (1992) are limited by their relatively poor resolution however, and further observations are required to confirm the nature of G63.7+1.1. Presented here are radio continuum and line, and high resolution far infrared data. The observations are discussed in Sec. 2 and the data presented in Sec. 3. In Sec. 4 the nature of G63.7+1.1 and its surroundings is discussed, and a model for the interaction between the two is presented. The paper is summarized in Sec. 5.

2. Observations

2.1. WSRT 1.4 GHz Observations

As noted above, the observations of Taylor et al. (1992) resolve G63.7+1.1 only poorly (resolution $1' \times 2'$ for an object $\sim 8'$ across). To improve our understanding of this object, G63.7+1.1 was imaged at higher resolution using the Westerbork Synthesis Radio Telescope (WSRT) at 1390 MHz. The observations are summarized in Table 1.

The total bandwidth of 80 MHz was split into eight separate bands, each 10 MHz wide, of which only the central six were usable. The data were edited and calibrated in the normal fashion at the WSRT and processed further using the Astronomical Image Processing System (AIPS); some errors, manifested as radial stripes centered on the brightest sources, remain in the data. Each 10 MHz band was self-calibrated, mapped, and CLEANed separately, then averaged to create the final maps. Images were made of Stokes parameters I, Q and U (Q and U maps were not cleaned).

2.2. IRAS Data

The infrared data presented here were collected by the Infrared Astronomical Satellite (IRAS; Beichman et al, 1988) and processed using the HiRes procedure at the Infrared Processing and Analysis Center (IPAC). The HiRes processing uses an iterative procedure based on the Maximum Correlation Method (Aumann et al 1990) and can produce images having resolution better than nominal for IRAS. However, the HiRes processing can drastically increase map artefacts such as striping, which becomes more prominent as the number of iterations (and the resolution) increases. The fluxes in the resulting maps are accurate to only about 25%, due largely to difficulty in determining the background level for the region of interest; this difficulty increases for regions, such as that presented here, which are close to the Galactic plane. The characteristics of the HiRes IRAS data presented here are listed in Table 2 together with integrated flux densities of the emission which we associate with G63.7+1.1.

2.3. CO Observations

A single observation of the Center for Astrophysics (CfA) 1.2m CO telescope (Cohen et al. 1986; Leung & Thaddeus 1992) was made towards G63.7+1.1 to look for molecular material possibly associated with G63.7+1.1. The spectrum covers 333 km/s at 0.65 km/s

channel separation and the rms fluctuations of the spectrum are 0.1 K. A sharp peak of strength ~ 0.65 K was found at ~ 11 km/s, and a broader and weaker peak of strength ~ 0.35 K was found near 23 km/s (all radial velocities are with respect to the local standard of rest).

Based on this spectrum, higher resolution ^{12}CO observations were made with the Five Colleges Radio Astronomy Observatory (FCRAO; Erickson et al 1992). Details of these observations can be found in Table 3. The background emission was removed by position switching to a nearby, presumed line-free, position on the sky at $\alpha = 19^h 47^m 56^s$, $\delta = 28^\circ 37' 31''$ (all equatorial coordinates in this paper are for epoch J2000).

2.4. DRAO HI Line Observations

The HI line data are from observations made at the Dominion Radio Astrophysical Observatory (DRAO; Roger et al 1973; Veidt et al 1985) in 1987. Some of the 21 and 74 cm continuum data have been published by Landecker et al. (1990) while the HI line data are presently unpublished. Relevant details for the HI data are recorded in Table 4. Information on large scale structure, missed by the DRAO synthesis telescope, is supplied by frequency-switched observations made with the DRAO 26m radio telescope. For more information on the observation see Landecker et al. (1990).

The region of interest falls near the edge of the field. The r.m.s. noise at map center is 0.9 K, but the primary beam correction raises it to 3.6 K for the region around G63.7+1.1.

3. Results

3.1. The WSRT 20 cm Data

G63.7+1.1 (Figure 1) is approximately 8' in diameter and is centered near $\alpha = 19^h 47^m 55^s$, $\delta = 27^\circ 44'$. G63.7+1.1 can be thought of as consisting of two components, a bright curved ridge running roughly from the south-east to the north-west, and a fainter diffuse plateau. The brightness of the plateau drops precipitously around much of the circumference of the object, but a shallower gradient exists in the south-east. The structure of the plateau has a rough bilateral symmetry around an axis running from the south-east to the north-west. A notch in the emission from G63.7+1.1, seen as a slight bay in the contours immediately to the south of a nearby compact source, appears in the north of the SNR. A faint tail of emission emerges radially from the center of the south-east region

of the object near a second nearby compact source; this tail is aligned with the bilateral symmetry axis of G63.7+1.1. While neither compact source can be definitely related to the SNR, it is interesting to note that the southern source is resolved, has a position-angle similar to that of the tail, and lies along the symmetry axis of the object.

The integrated flux density of G63.7+1.1 is 1.63 ± 0.06 Jy at 1.39 GHz. The quoted uncertainty is strictly internal, and does not include any possible systematic effects. A number of flux density values at other frequencies are listed in Table 5. Earlier observations were made with lower resolution and the two nearby compact sources are included in those flux determinations. If those sources are included in our measurements the total integrated flux density is 1.76 ± 0.01 Jy, consistent with previous data.

Combining our data with the flux density measurements listed in Table 5 we calculate a spectral index (α , $S_\nu \propto \nu^\alpha$) of $\alpha = -0.28 \pm 0.02$ between 0.408 and 10.55 GHz (systematic effects will probably result in a larger uncertainty than quoted here) with a possible flattening at lower frequencies. Since the two nearby compact sources are probably extragalactic, with steep negative spectral indices, the actual spectral index may be marginally flatter than that calculated here. Nonetheless, this spectral index demonstrates that the emission from G63.7+1.1 is non-thermal in nature (i.e. probably synchrotron emission), a conclusion confirmed by the detection of polarized emission within the object..

Figure 2 presents vectors corresponding to the linearly polarized emission from G63.7+1.1, smoothed to $30''$, superposed upon contours of the total intensity data. The average level of polarization across the object is 7%, reaching a maximum of 16% in the north. The level of polarization is lower to the south-east than to the north-west, suggesting greater depolarization of the emission to the south-east. The polarization vectors associated with the brightest emission are oriented perpendicular to the ridge. The vectors associated with the plateau region to the north and north-west are radial, while the vectors in the region in between are circumferential. The differences in orientation of these vectors suggest either that G63.7+1.1 has an intrinsically complex magnetic field structure or that there are significant Faraday rotation differences across the face of the remnant.

3.2. The IRAS data

The HiRes IRAS data are presented in Fig. 3. At 12 and $25 \mu\text{m}$ the emission within the SNR is concentrated near the radio peak in the center of the SNR, while at 60 and $100 \mu\text{m}$ it lies predominately to the south and east of the peak; the 60 and $100 \mu\text{m}$ emission appears to form a bowl in which G63.7+1.1 sits. The emission from these two areas is

not spatially distinct, and independent fluxes for each region cannot be obtained. Some compact emission lies to the west of the remnant at 60 and $100\mu\text{m}$.

The color corrected flux densities for the emission which lies inside the radio contours are listed in Table 2. Assuming a $\lambda^{1.5}$ emissivity law, color temperatures of $T_{12/25} = 183$ K, $T_{25/60} = 62$ K, and $T_{60/100} = 27$ K are found with uncertainties on the order of 30%. A similar wide variation in the color temperatures is seen in “old” SNRs (Saken et al. 1992; Arendt 1989), where the typical “old” SNR has $T_{12/25} = 150$ K, $T_{25/60} = 60$ K, and $T_{60/100} = 30$ K (younger SNRs tend to have spectra which are reasonably well fit by a single temperature, ~ 90 K). This result is based on a statistical study of all IRAS-detected SNRs, however, and may not be strictly applicable to FC SNRs.

3.3. The FCRAO CO Data

The major CO features found in the FCRAO CO data, for the velocity range from approximately -3 km/s to 24 km/s, are shown in Figure 4. Three images, chosen to show five CO features labeled A-E, are presented here.

-4.7 to -2.1 km/s Feature A consists of a faint arc of CO in the NE portion of the field.

It is spatially separate from G63.7+1.1 and does not appear connected to it in any way.

8.3 to 13.5 km/s Feature B is a horseshoe shaped feature, centered near $\alpha = 19^h 48^m 7^s$, $\delta = 27^\circ 38' 38''$, roughly $8'$ in diameter. The NW edge of the feature crosses the southern part of G63.7+1.1. Interestingly, a gap in the structure coincides with the position of the continuum “tail” emanating from the south-east edge of the SNR.

10.9 to 16.1 km/s Feature C appears to the north-west of G63.7+1.1, adjacent to the edge of the SNR. It is not clear if this CO is physically associated with the G63.7+1.1.

18.7 to 23.9 km/s Feature D appears near the bottom of G63.7+1.1 roughly coincident with infrared emission at 60 and $100\mu\text{m}$. It is interesting to note that Feature D is coincident in position with the gap seen in the north-west of Feature B.

21.3 to 26.5 km/s Feature E lies in the extreme south-east of the observed field. Once again there does not seem to be any evidence of a link between this CO and G63.7+1.1 and there will be no further discussion of this feature.

3.4. The DRAO HI Data

After the detection of molecular material possibly associated with G63.7+1.1, the DRAO HI data cube was searched for indications of atomic material, in the same velocity range, which might also be associated with the SNR. In Fig. 5 the HI data for the region around G63.7+1.1 for the velocity range 11 to 47 km/s are presented. The average emission has been subtracted from each channel for presentation purposes and the data have been smoothed to 2.1' circular resolution and 3.3 km/s velocity separation.

While there is no HI emission, above the local background, at the extremes of the velocity range shown, emission at the edges of G63.7+1.1 is seen in the central velocity maps. A plot of the average HI emission over the velocity range 14 to 37 km/s is presented in Figure 6. The HI traces the upper boundary of G63.7+1.1 reasonably well. The brightest HI to the northeast runs parallel to the edge of the SNR, as does much of the emission to the north-west (although some of the brightest emission is separated from the remnant, faint emission above background lies adjacent to the SNR edge); with the present resolution there is no separation between the outer continuum boundary of the SNR and these HI features. The apparent spatial correlation between the HI emission and the region where the continuum emission has the steepest intensity gradient suggests that the emission is physically associated with G63.7+1.1. HI within the SNR boundary, seen especially at ~ 30 km/s, is adjacent to CO Feature D, but differs in velocity by ~ 10 km/s..

The average brightness temperature of the HI (above background) is $T_B = 2.9 \pm 0.7$ K. Assuming a distance to G63.7+1.1 of 3.8 ± 1.5 kpc (see Discussion) the average column density of the HI, $N_{HI} = 4.4 \pm 1.3 \times 10^{19}$ cm $^{-2}$, implies a mass of $M_{HI} = 51 \pm 43$ M $_{\odot}$. The uncertainty in the mass is due mostly to the uncertainty in the distance estimate.

4. Discussion

4.1. The Nature of G63.7+1.1

With the observations presented here we are able to test the classification (Taylor et al. 1992) of G63.7+1.1 as a FC SNR. An object is generally classified as a FC SNR if it has a flat, non-thermal, spectral index, a centrally brightened radio morphology, and no indication of an associated limb-brightened shell. The spectral index and polarization discussed in Sec. 3.1 demonstrate that the emission process is indeed non-thermal. From Figure 1 it is clear that G63.7+1.1 shows a centrally brightened radio morphology (illustrated also in Figure 7, discussed in detail later). There is no evidence of a limb-brightened shell outside

G63.7+1.1 to a level of $\Sigma_{1GHz} \sim 2 \times 10^{-22} \text{ W m}^{-2} \text{ Hz}^{-1} \text{ sr}^{-1}$ (the level of the residual uncleaned grating rings), assuming a spectral index of -0.5 for any shell emission. A similar limit is calculated from the data of Taylor et al. (1996). Thus the minimal criteria for classification as a FC SNR are met and we interpret the object as a pulsar-powered nebula (although no pulsar has yet been detected in the SNR).

It is possible, however, to find these same observational traits in objects known as “interacting composites,” objects in which a pulsar has caught up to, and is interacting with, the SNR shell created in the same explosion as the pulsar (Shull et al. 1989). This class of objects is of necessity associated with fast moving pulsars, and the resulting nebulae reflect this with a distinct bow shock morphology oriented along the direction of motion of the pulsar. In addition, there is usually an indication of the existence of the SNR shell, either in the form of “wings” of emission associated with the FC nebula (e.g. CTB80, Safi-Harb et al. 1995), or as a fully formed shell located near the FC nebula (e.g. G5.4-1.2; Frail & Kulkarni 1991). G63.7+1.1 shows no indication of either of these phenomena. While part of G63.7+1.1 has distinctly sharper edges than the rest, the characteristic “v”-shape of a bow-shock is not present. Similarly, there is no indication of an associated SNR shell in either the 20cm data presented here, nor in the wider field 92cm data of Taylor et al. (1996). Consequently, we conclude that G63.7+1.1 is not an interacting composite SNR.

4.2. The Morphology of G63.7+1.1

The steep intensity gradient at the edge of the northern section of the remnant, compared to the shallow gradient to the south-east, suggests an interaction between the SNR and its surrounding ISM. To better illustrate the nature of the sharp intensity gradient, the SNR was divided into 12 sectors, each 30° wide, and an average radial profile for each sector was derived. Figure 7 shows two average intensity profiles through the SNR. The shallower profile (Fig. 7a) is centered to the south (at 6 o’clock), while the steeper profile (Fig. 7b), typical of the profiles taken from the northern portion of the SNR, is centered to the west (at 3 o’clock). The southern profile declines smoothly to zero and is essentially featureless while the western profile reaches a plateau at $\sim 4 \text{ mJy/beam}$ before the brightness drops to zero. The region over which the brightness drops from 4 mJy to zero in Fig. 7b is spatially unresolved. The difference in distance, from assumed SNR center, at which the two profiles reach zero reflects the asymmetric morphology of the SNR.

Assuming optically thin emission, the brightness distribution within the remnant is a function of the volume emissivity distribution and the observed path-length through the SNR. As the path-length presumably decreases towards the edge of the SNR, a uniform

or radially decreasing emissivity should result in the brightness decreasing towards the edge. The constant brightness across the plateau implies an emissivity which increases with radius, an interpretation that is at odds with the commonly accepted view of FC SNRs as homogeneous bubbles of synchrotron emitting material (e.g. Pacini & Salvati 1973; Reynolds & Chevalier 1984).

The emissivity was explored quantitatively by deconvolving the 2-D brightness distribution with the assumed 3-D shape of the SNR (Leahy & Volk 1994; Leahy 1991) using software kindly provided by D.A. Leahy. The emissivity profiles resulting from the intensity profiles of Figure 7 are presented in Figure 8. The emissivity profile for the southern sector (Fig. 8a) shows a peak at or near the center of the SNR, followed by a slow decline towards the edge of the SNR. The profile for the western wedge (Fig. 8b) also shows the central emissivity peak, but with a secondary emissivity peak near the edge of the SNR. Most of the other emissivity profiles (not shown) also exhibit this peak in emissivity towards the edge of the SNR, although to lesser extents.

The rise in emissivity towards the edge of the SNR can be explained in two ways, both of which imply an interaction between the SNR and its environment. Assuming a particle energy distribution of the form $N(E) = N_o E^{-\gamma}$ (where E is the electron energy, $N(E)$ the number of electrons with that energy, and N_o and γ constants), the volume emission coefficient (ϵ_ν) is given by

$$\epsilon_\nu = f(\gamma) N_o \nu^{1-\gamma/2} (B \sin \theta)^{\gamma+1/2} \quad (1)$$

(Pacholczyk 1970) where θ is the pitch angle of the electrons, B the magnetic field intensity, and $f(\gamma)$ is a complicated function of γ . An increase in either the magnetic field strength or the particle energy distribution (by modifying either N_o or γ) can then result in an increase in the volume emissivity.

The magnetic field strength can be increased if the SNR is interacting with the ISM and compressing the ambient magnetic field. Additionally, an interaction between the SNR and the ISM may result in the creation of a second population of relativistic particles at the edge of the SNR. If G63.7+1.1 is similar to the Crab Nebula, the detected nebula is bounded by a thin shell of slow-moving (10^3 km/s) SN ejecta which drives a blast wave into the surrounding ISM. The interaction between the blast wave and the ISM may produce relativistic particles near the shock as for a shell SNR. This would result in increased numbers of emitting particles at the outer boundary of the synchrotron nebula, as compared to the interior of the nebula, thus increasing the emissivity as required.

This second scenario raises an interesting possibility. The power index of the particle energy distribution, γ , is different for particles produced by the pulsar and for those

produced by the interaction with the ISM (for the pulsar accelerated particles $\gamma \sim 1.4$, for the shock accelerated particles, $\gamma \sim 2$). This second population of particles should then result in an observable spectral steepening at the edge of G63.7+1.1, similar to that found in the composite SNR G18.95-1.1 (Fürst et al 1997). If such steepening exists then G63.7+1.1 will, at some frequency, show limb-brightening, suggesting that G63.7+1.1 may be undergoing a transition from FC to composite SNR, providing the “missing link” between these two classes of objects.

We interpret the rise in emissivity as a result of the interaction between the synchrotron nebula and the ISM, and *not* as a result of an interaction between a fast moving halo of ejecta and the ISM. A blast wave associated with fast moving ejecta would have disrupted the surrounding material and swept it away from the synchrotron nebula. While recombined HI has been found behind the shock in W44 (Koo & Heiles 1995) the blast wave which ionized the material is easily visible; this is clearly not the case with G63.7+1.1, supporting our interpretation.

4.3. A Model for G63.7+1.1

Our information on the ISM comes from three sources: the FIR, CO and HI data, probing the dust, molecular and atomic components respectively. Much of the emission in these data is spatially coincident with G63.7+1.1. While it can be argued that these coincidences are the result of chance superposition of unrelated features along the line of sight to the SNR, several aspects of the data argue for a physical connection between the SNR and its surrounding ISM.

To illustrate this connection Fig. 9 shows contours of the emission from the radio continuum, $100\mu m$, and CO feature D. The FIR emission provides the strongest argument for an association. At 60 and $100\mu m$ the emission forms a bowl around the bottom of the G63.7+1.1, with the northern edge of the emitting region lying adjacent to the southern extreme of the bright radio continuum ridge. At $100\mu m$ a finger of emission extending to the northwest is seen near $\alpha \sim 19^h 45^m$, $\delta \sim 27^\circ 43'$; this finger lies adjacent to the bright ridge, and extends in the same direction (Fig 9). A similar finger is seen in CO feature D. Combined with the color temperatures of the dust emission, which are consistent with the shocked dust associated with other SNRs, these characteristics suggest a causal relationship between the FIR emitting material, CO Feature D, and the SNR.

These aspects of the data provide compelling arguments for an association between G63.7+1.1 and molecular material to the south. The HI data provide additional, albeit

weaker, support for this association. The agreement in morphology between the partial HI shell seen in Fig. 6 and G63.7+1.1 argues for a relationship between the two. In addition, the faint HI emission seen interior to the SNR at $v \sim 30$ km/s lies adjacent to CO Feature D; this feature could be unrelated, or it could be molecular material from Feature D which has been dissociated and ionized by the interaction with G63.7+1.1, and which has then recombined. While this would explain the velocity shift between the HI and CO emission, the small size of this velocity shift suggests that the material has been accelerated only a small amount, implying that the shock associated with the interaction was weak. In turn, this suggests that any spectral steepening associated with the SNR/ISM interaction may be small. The large noise in the HI data do not allow us to say anything more about this possibility.

In short, we feel that these observations show that G63.7+1.1 is indeed interacting with its surroundings and allow us to present the following observational scenario.

The SNR G63.7+1.1 lies adjacent to molecular material to the south (Feature D at 21 km/s) with which it has interacted. The SNR shock has heated some of the dust associated with the molecular material, giving rise to the FIR emission. The shock has dissociated and ionized some fraction of the molecular material, accelerating it in the process by $v \sim 10$ km/s, and the recombined material gives rise to the faint HI emission seen interior to the SNR. The HI to the north of the remnant at these same velocities mimics the morphology of the SNR, possibly the result of the interaction between the SNR and the surrounding atomic material. The expansion of the SNR is truncated to the south-west by its interaction with the molecular material, while the HI forms a “helmet” surrounding the SNR in all other directions. The projection of the FIR and CO emission within the SNR suggests that the whole system is inclined at an angle to the plane of the sky, resulting in the observed morphology. The situation is similar to that described for another FC SNR, G74.9+1.2 (Wallace et al. 1997). That SNR lies near an HI shell which defines the inner edge of an interstellar cavity; on one side the pulsar powered nebula expands freely into the low density inside the cavity, but on the other side the HI shell impedes the expansion.

This model allows us to calculate a distance to G63.7+1.1 based upon the radial velocity of the associated ISM. The central velocity of both the HI ($v \sim 25$ km/s) and CO Feature D ($v \sim 21$ km/s) are close to the velocity of the tangent point in this direction ($v = 22.4$ km/s). The velocity ranges quoted for both the CO and HI data extend beyond this velocity, suggesting that G63.7+1.1 lies at or near the tangent point. Assuming a flat rotation curve ($R_\odot = 8.5$ kpc and $V_\odot = 220$ km/s) the distance to the tangent point is 3.8 ± 1.5 kpc; the velocity at which CO Feature D is first seen (18.7 km/s) corresponds to a kinematic distance of either 2.3 or 5.3 kpc, for the near and far sides of the tangent point

distance respectively, leading to the large uncertainty. The linear diameter of G63.7+1.1 is then 8.8 pc and the luminosity 4.3×10^{-21} W Hz $^{-1}$.

Situations such as we propose for G63.7+1.1 are modeled by Arthur & Falle (1991, 1993) who suggest that the remnant of a SN which explodes near a density discontinuity, such as the edge of a molecular cloud, will be roughly elliptical, with the SNR penetrating further into the low density region than into the high density region. The symmetry axis of the remnant will be perpendicular to the plane of the density interface. These aspects of the model agree with the observed morphology of the SNR and with its location relative to CO feature D.

The models of Arthur and Falle predict the presence of a jet of material, “squirted” from the high density region into the low, near the symmetry axis of the SNR. Such an effect may be responsible for the observed bright ridge along the symmetry axis of G63.7+1.1. If molecular material has been squirted into the interior of the SNR, as suggested by Fig 9, then some portion of it may be expected to be dissociated and ionized, providing additional particles which can contribute to the radio continuum emission to form the observed ridge. If this is the case then emission associated with the ridge may have higher Faraday rotation than the rest of the remnant due to the presence of a large amount of ionized material. Radio emission from the south-eastern portion of the SNR may be depolarized by strong Faraday rotation associated with dense ionized material created as the SNR interacts with the molecular material to the south; it is interesting to note that the 60 μ m FIR emission appears to delineate the region of strongest depolarization. This depolarization would imply that the molecular material must be on the near side of the SNR, and that the SNR is inclined away from the observer. Measurements of the intrinsic magnetic field orientation and the rotation measure of the SNR based on radio polarimetry at short wavelengths may help cast light on these issues.

The tail of emission to the south-east may be similar to the Crab Nebula’s chimney, and may arise from the same process (e.g. Cox et al 1991). However, if the SNR is interacting with CO Feature B (instead of, or in addition to, Feature D, as assumed elsewhere in the paper) an additional possibility arises. It has been noted that the “tail” coincides in position with a “gap” in the CO feature. The tail may be the result of SN ejecta being impeded by the molecular cloud but escaping through the gap.

4.4. Implications

Two pieces of evidence suggest strongly that G63.7+1.1 is interacting with the surrounding ISM. First, there is the steep intensity gradient around much of the perimeter of the SNR. Second, there is the striking emission at 60 and $100\mu\text{m}$ which bears a strong morphological resemblance to the SNR; the fingers of emission seen in the $100\mu\text{m}$ data and in CO Feature D, both of which extend in the same direction as the radio continuum ridge, add further support to this suggestion. The apparent interaction between G63.7+1.1 and the surrounding interstellar material illustrates that this FC SNR is *not* expanding into a low density region of the ISM. This makes G63.7+1.1 the second FC SNR for which this can be said (the first is G74.9+1.1; Wallace et al. 1997) and has important implications for our understanding of the nature of FC SNRs.

Chevalier (1977) invoked low density ISM to explain the absence of shells associated with FC SNRs. The assumption made is that no emission will be detectable if the blast wave associated with a fast moving halo of ejecta has encountered only a small amount of material. However, it has been shown that G63.7+1.1 and G74.9+1.2 do not lie in low density regions of the ISM. This implies directly that both these objects are not surrounded by fast moving halos of ejecta, and thus that Chevalier's (1977) model is not applicable for them (although it may still hold for other FC SNRs). Since most models of FC SNRs (e.g. Reynolds & Chevalier 1984; Kennel & Coroniti 1984) assume that they are surrounded by fast moving ejecta, a refutation of Chevalier's hypothesis demands a rethinking of even our most basic understanding of these objects.

5. Conclusion

High resolution radio continuum observations of the SNR candidate G63.7+1.1 have been presented, along with far-infrared, HI, and CO observations of its surroundings. These observations show that G63.7+1.1 has a centrally-brightened radio morphology with no detectable limb brightening; no limb brightened shell is seen down to a level of $\Sigma_{1\text{ GHz}} \sim 2 \times 10^{-22} \text{ W m}^{-2} \text{ Hz}^{-1} \text{ sr}^{-1}$. The spectral index of the emission, $\alpha = -0.28 \pm 0.02$, along with the detection of polarization, imply a non-thermal emission process. G63.7+1.1 is thus most likely a filled-center SNR.

The morphology of G63.7+1.1 can be broken down into two components, a bright resolved core and a fainter, more uniform, plateau. The plateau is shown to have a sharp, unresolved, intensity gradient marking its outer edge around most of the remnant, but exhibits a much shallower gradient to the south-east. Modeling of the emissivity profile

within the remnant suggests that an increase in emissivity must occur around the portions of the remnant having a sharp intensity gradient. This rise in emissivity implies an increase in magnetic field strength, the injection of additional emitting particles, or both, at the edges of the SNR. This may suggest that G63.7+1.1 is in the process of forming a limb-brightened component at its edges and may thus be in transition from FC to composite SNR.

The observations of the ISM around G63.7+1.1 suggest that the remnant lies adjacent to molecular material with which it is interacting. Some of this molecular material may have been injected into the SNR interior, perhaps creating a ridge of brighter radio emission with associated features seen at $100\mu\text{m}$ and in CO Feature D. The radial velocity of the molecular material with which the SNR is interacting indicates that the SNR lies at or near the tangent point of the Galactic rotation curve in this direction, implying a distance to the remnant of 3.8 ± 1.5 kpc.

The interaction between G63.7+1.1 and the ISM implies both that the SNR is *not* lying in a low density region of the ISM, and that the SNR is *not* surrounded by a fast moving halo of ejecta. This result demands a rethinking of models used to describe FC SNRs and their evolution.

The authors would like to thank Daniel Puche for obtaining the CfA spectrum towards G63.7+1.1. Gerald Moriarity-Schieven is acknowledged for his invaluable assistance in obtaining the FCRAO data. Grateful thanks are offered to Mark Heyer for obtaining additional FCRAO data for the authors. Thanks are also due to Denis Leahy for provision of the software used in Sec. 4, and to Wolfgang Reich for providing his 4.85 and 10.55 GHz flux densities. The Dominion Radio Astrophysical Observatory is operated as a national facility by the National Research Council of Canada. This research was supported in part by a grant from the Natural Sciences and Engineering Research Council of Canada.

REFERENCES

Arendt, R. G. 1989, *ApJS*, 70, 181.

Arthur, S.J., Falle, S.A.E.G., 1991, *MNRAS*, 251, 93

Arthur, S.J., Falle, S.A.E.G., 1993, *MNRAS*, 261, 681

Aumann, H.H., Fowler, J.W., and Melnyk, M., 1990, *AJ*, 99, 1674

Beichman, C.A., Neugebauer, G., Habing, H.J., Clegg, P.E., Chester, T.J., 1988, *IRAS Catalogs and Atlases: Explanatory Supplement*, GPO, Washington, D.C.

Chevalier, R.A., 1977, In *Supernovae*. D.N. Scramm (ed.), Dordrecht: Reidel, 53

Cohen, R.S., Dame, T.M., Thaddeus, P., 1986, *ApJS*, 60, 695

Cox, C.I., Gull, S.F., Green, D.A., 1991, *MNRAS*, 250, 750

Erickson, N.R., Goldsmith, P.F., Novak, G., Grosslein, R.M., Viscuso, P.J., Erickson, R.B., Predmore, C.R., 1992, *IEEE Trans. Microwave Theor. Tech.*, 40, 1

Frail, D.A. and Kulkarni, S.R., 1991, *Nature*, 352, 785

Fürst, E., Reich, W., Aschenbach, B., 1997, *A&A*, 319, 655

Green D.A., 1996, ‘A Catalogue of Galactic Supernova Remnants (1995 July version)’, Mullard Radio Astronomy Observatory, Cambridge, United Kingdom (available on the World-Wide-Web at “<http://www.phy.cam.ac.uk/www/research/ra/SNRs/snrs.intro.html>”).

Kennel, C.F., Coroniti, F.V., 1984, *ApJ*, 283, 694

Koo, B-C., Heiles, C., 1995, *ApJ*, 422, 679

Landecker, T.L., Clutton-Brock, M., Purton, C.R., 1990, *A&A*, 232, 207

Leahy, D.A., 1991, *A&A*, 247, 584

Leahy, D.A., Volk, K., 1994, *A&A*, 282, 561

Leung, H.O., Thaddeus, P., 1992, *ApJS*, 81, 267

Pacini, F., Salvati, M., 1973, *ApJ*, 186, 249

Pacholczyk, A.G., “Radio Astrophysics,” W.H. Freeman and company, San Francisco, 1970

Reynolds, S.P. and Chevalier, R.A., 1984, *ApJ*, 278, 630

Roger, R.S., Costain, C.H., Lacey, J.D., Landecker, T.L., Bowers, F.K., 1973, *Proc. IEEE*, 61, 1270

Romani, R.W., Reach, W.T., Koo, B.C., and Heiles, C., 1990, *ApJ*, 349, L51

Safi-Harb, S., Ogelman, H., Finley, J.P., 1995, *ApJ*, 439, 722

Saken, J.M., Fesen, R.A., Shull, J.M., 1992, *ApJS*, 81, 715

Shull, J.M., Fesen, R.A., Saken, J.M., 1989, *ApJ*, 346, 860

Taylor, A.R., Wallace, B.J., Goss, W.M., 1992, *AJ*, 103, 931

Taylor, A.R., Goss, W.M., Coleman, P.H., van Leeuwen, J., Wallace, B.J., 1996, *ApJS*, 107, 239

Veidt, B.G., Landecker, T.L., Vaneldik, J.F., Dewdney, P.E., Routledge, D., 1985, *Radio Sci.*, 20, 1118

Wallace, B.J., Landecker, T.L., Taylor, A.R., 1994, *A&A*, 286, 565

Wallace B.J., Landecker T.L., Taylor A.R., Pineault S., 1997, *A&A*, 317, 212

Fig. 1.— The large extended feature in the middle of the map is G63.7+1.1. The contours are at -0.2 (dashed), 0.2, 0.6, 1.0 mJy/beam and upwards in steps of 1 mJy/beam thereafter. Note the two compact sources to the north and south-east of the remnant as well as the artefacts emanating radially from the bright compact source to the south-west.

Fig. 2.— The lines denoting polarized electric field intensity and position angle are superposed upon the contours from the total intensity data. The polarization data has been smoothed to 30" circular resolution while the total intensity contours are at full resolution. The position angle of the lines denotes the direction of the electric field vectors, and a vector of length 1' corresponds to a linearly polarized intensity of approximately 1 mJy/beam.

Fig. 3.— The upper panels show the 12 and 25 μ data in greyscale (left and right respectively) while the lower show the 60 and 100 μ . Contours from the WSRT 1390 MHz continuum image are overlaid for reference.

Fig. 4.— The FCRAO CO data are presented in greyscale, with contours of the WSRT continuum image overlaid for reference. The top figure is the average of two channels while the bottom two figures are three channel averages centered on the velocities indicated. The greyscale runs from -0.3 to +0.7 K, the contours run from 1 to 19 mJy/beam in steps of 2 mJy/beam. The features labeled in the plot are discussed in the text.

Fig. 5.— The greyscale, denoting HI emission, ranges from 30 K below the background (white) to 25 K above (black). Overlaid are contours of the WSRT 1390 MHz continuum image. The central velocity of each image is indicated.

Fig. 6.— The HI emission (greyscale) averaged over velocities 14 to 37 km/s; overlaid are contours from the WSRT 21cm data. The most intense HI emission lies around the northern edge of the SNR.

Fig. 7.— Two intensity profiles through G63.7+1.1. Profile A is from a sector centered on the southern portion of the remnant, while B is from the western portion. Notice that the intensity reaches a plateau in B at \sim 4 mJy/beam.

Fig. 8.— The emissivity profiles derived from the intensity profiles presented in the previous figures. Notice that the secondary emissivity peak at \sim 3' in B is not seen in A. Arbitrary units are used for the emissivity scale.

Fig. 9.— Contour plots of the radio and 100 μ m emission, along with that associated with CO Feature D. The line extending from south-east to north-west was chosen to match the finger of 100 μ m emission discussed in the text. The perpendicular line was chosen to pass through the peak of the 100 μ m emission. Features parallel to the 100 μ m finger can be seen

in the radio continuum and in CO Feature D.

Table 1. Summary of WSRT 1390 MHz Observations Towards G63.7+1.1

Field Center	$\alpha(J2000) = 19^h 45^m 55.0^s$
	$\delta(J2000) = 27^\circ 36' 30.0''$
Bandwidth (observed/used)	80/60 MHz
Resolution (RA \times Dec)	$13.8'' \times 26.4''$
RMS deviations	$50 \mu\text{Jy}/\text{beam}$
Shortest Baseline	36m
Largest Detectable Structure	$\sim 20'$

Table 2. IRAS Data for G63.7+1.1

	12μ	25μ	60μ	100μ
Resolution (RA \times Dec)	$2.5' \times 1.0'$	$1.6' \times 0.5'$	$2.75' \times 1.1'$	$2.8' \times 2'$
Iterations	1	5	5	20
Color Corrected Fluxes (Jy)	5.7 ± 1.0	6.3 ± 1.2	28.8 ± 2.5	105 ± 33

Table 3. Summary of FCRAO ^{12}CO Observations Towards G63.7+1.1

Field Center	RA(J2000)	$19^h 47' 57.5''$
	Dec(J2000)	$27^\circ 44' 0.8''$
Field Size	RA \times Dec	$20.^{\circ}9 \times 20.0'$
Resolution		$50.2''$
Beam Spacing		$25.1''$
Central Velocity		20 km/s
Number of Channels		32
Channel Separation		2.60 km/s
Integration time		60s
per point		

Table 4. DRAO HI Observations Towards G63.7+1.1

Field Center	RA(J2000)	19 ^h 46 ^m 18.3 ^s
	Dec(J2000)	28°42'23.4"
Synthesized Beam	RA × Dec	1.'0 × 2.'1
Smoothed Resolution	RA × Dec	2.'1 × 2.'1
Central Velocity		-24.7 km/s
Channel Separation		1.65 km/s
Polarization		RHCP
Observation date		1987

Table 5. Measured Radio Flux Densities for G63.7+1.1

Frequency	Flux Density	Uncertainty
327 ^a	1.47	0.04
408 ^b	2.1	0.2
1390 ^c	1.63	0.06
1420 ^b	1.71	0.02
2695 ^d	1.41	0.1
4850 ^e	1.16	0.10
10550 ^e	0.95	0.05

^aValue obtained by the authors from the data of Taylor et al. 1996

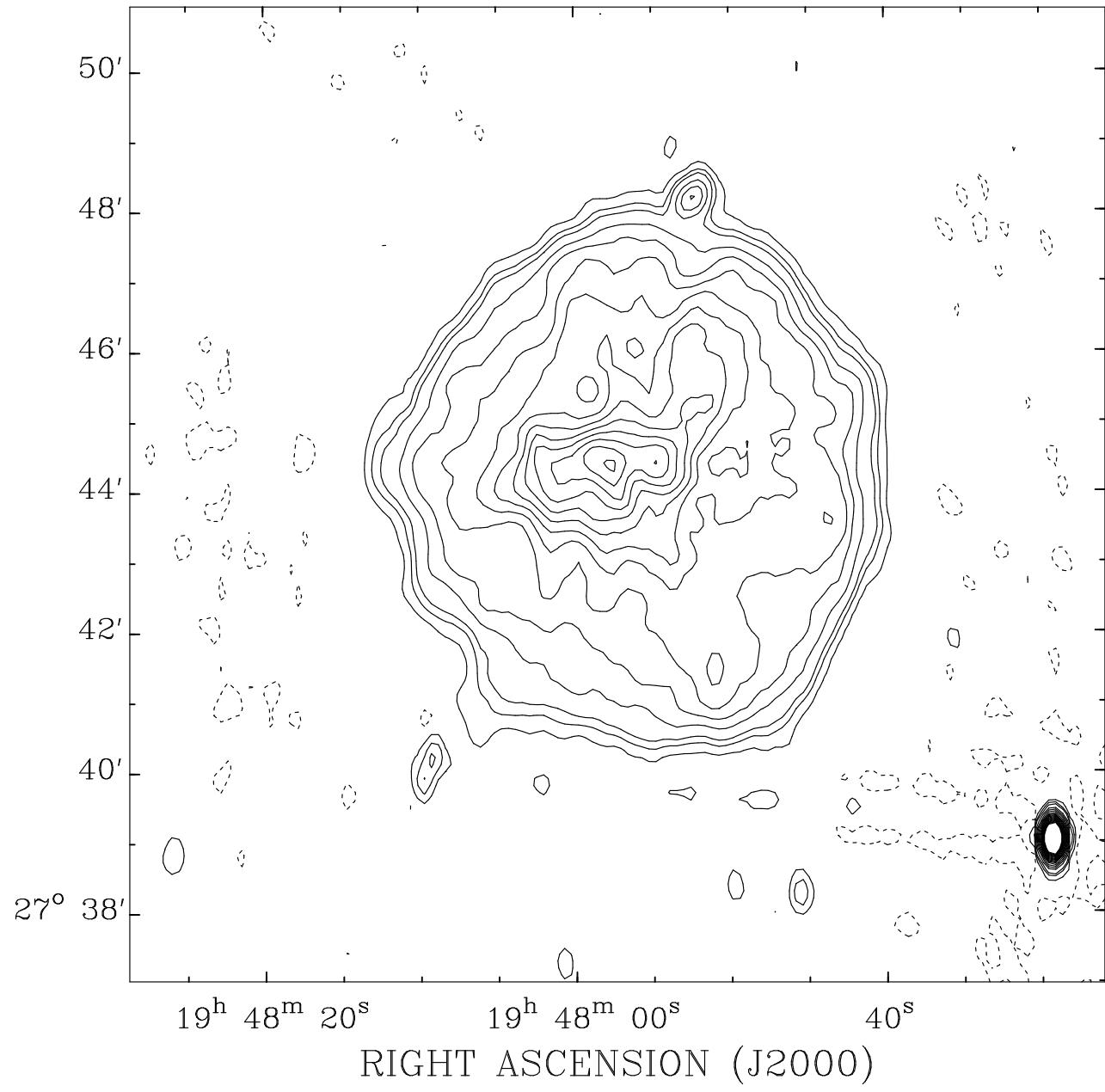
^bValue obtained by the authors from unpublished data of Landecker et al. 1990

^cThis paper

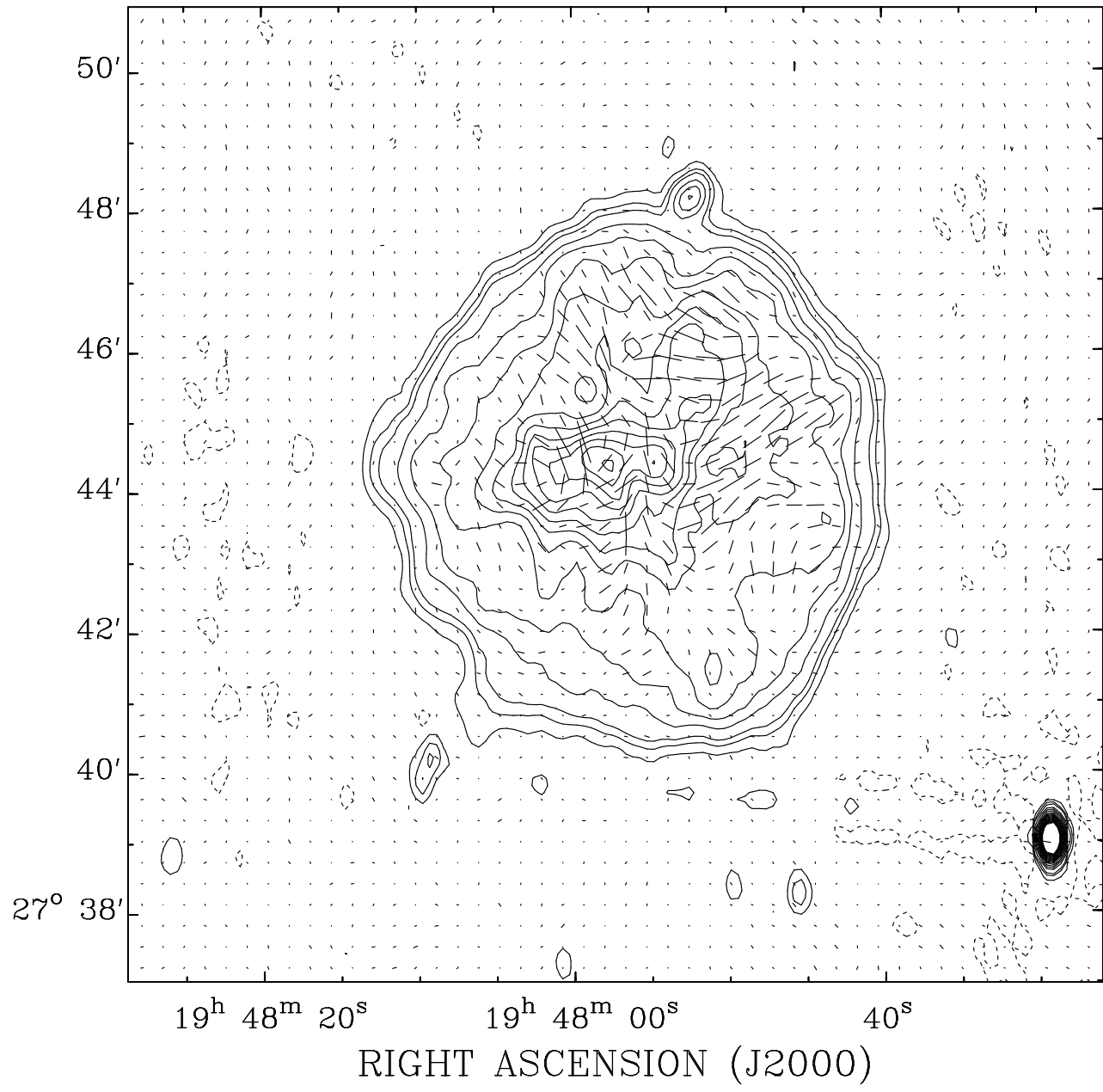
^dValue obtained by the authors from the data of Reich et al. 1990

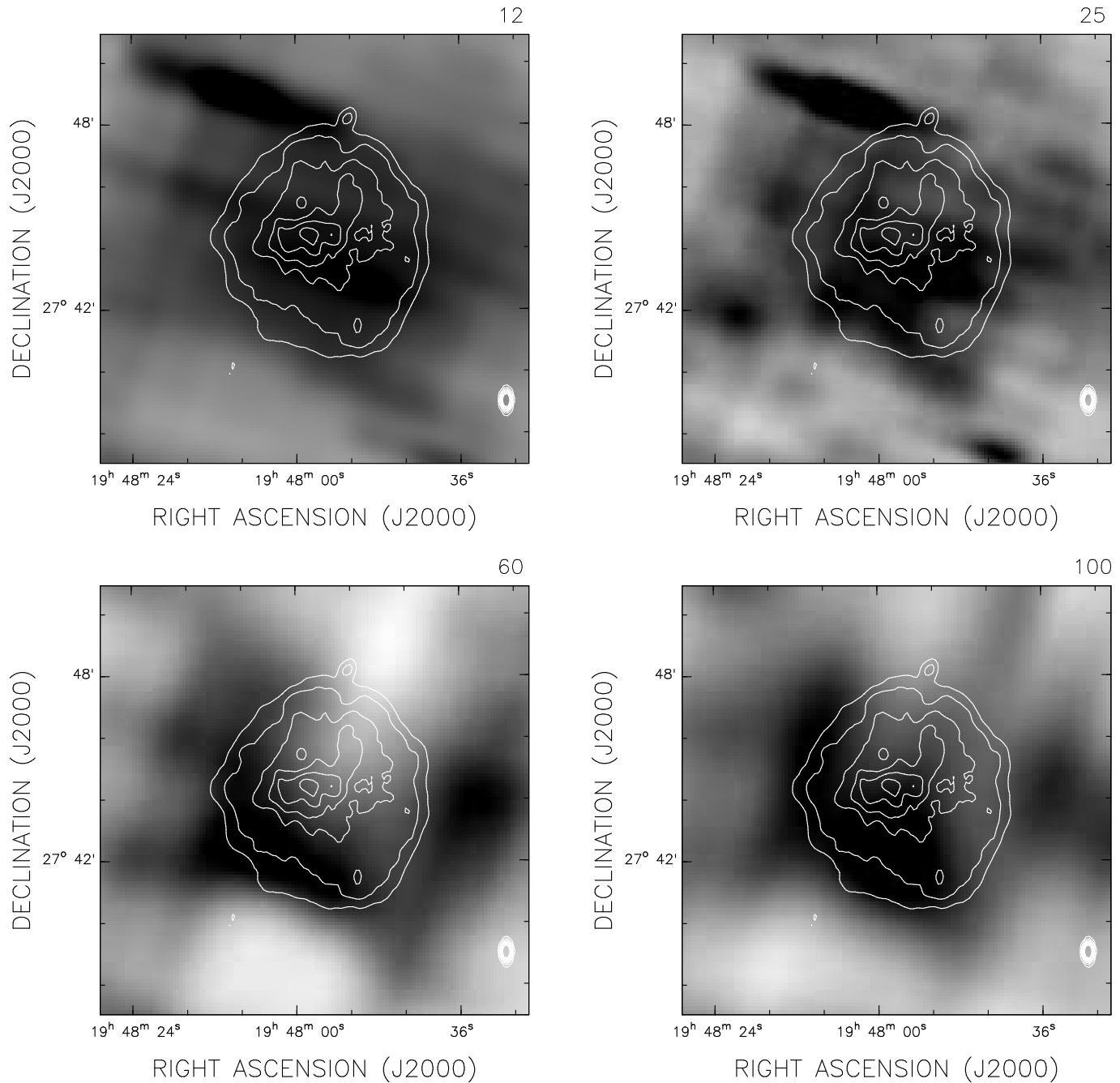
^eW. Reich (private communication)

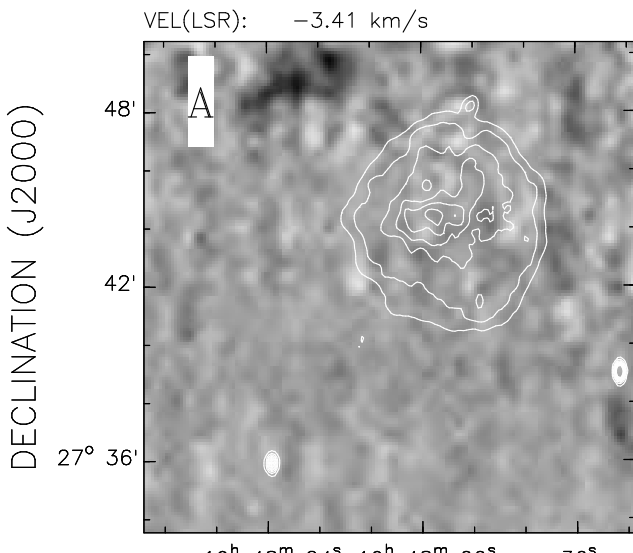
DECLINATION (J2000)



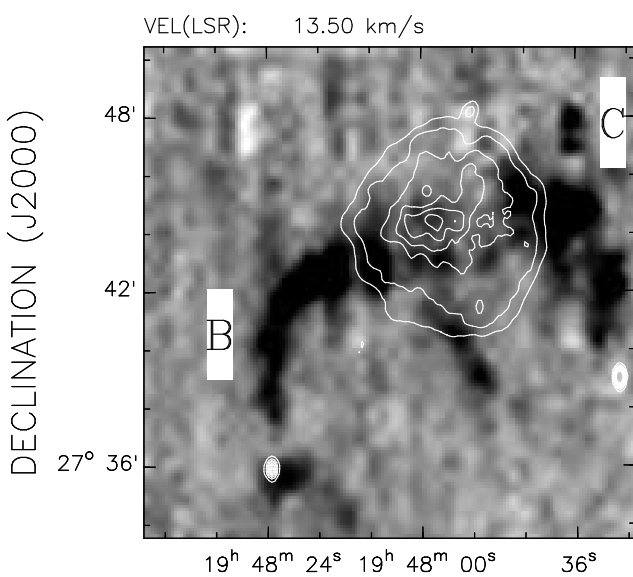
DECLINATION (J2000)



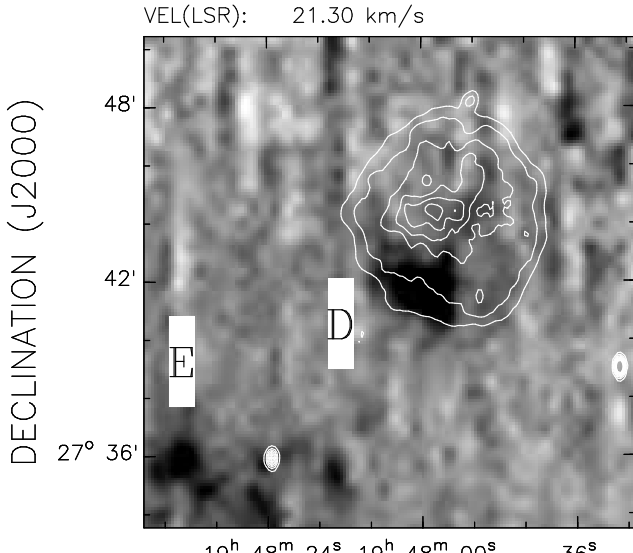




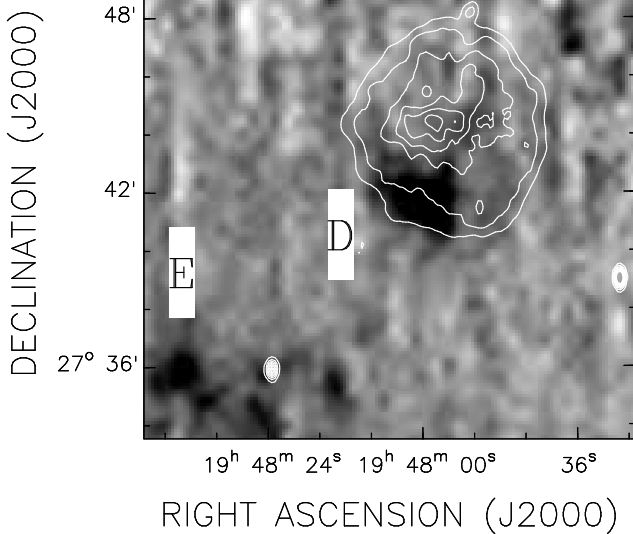
RIGHT ASCENSION (J2000)



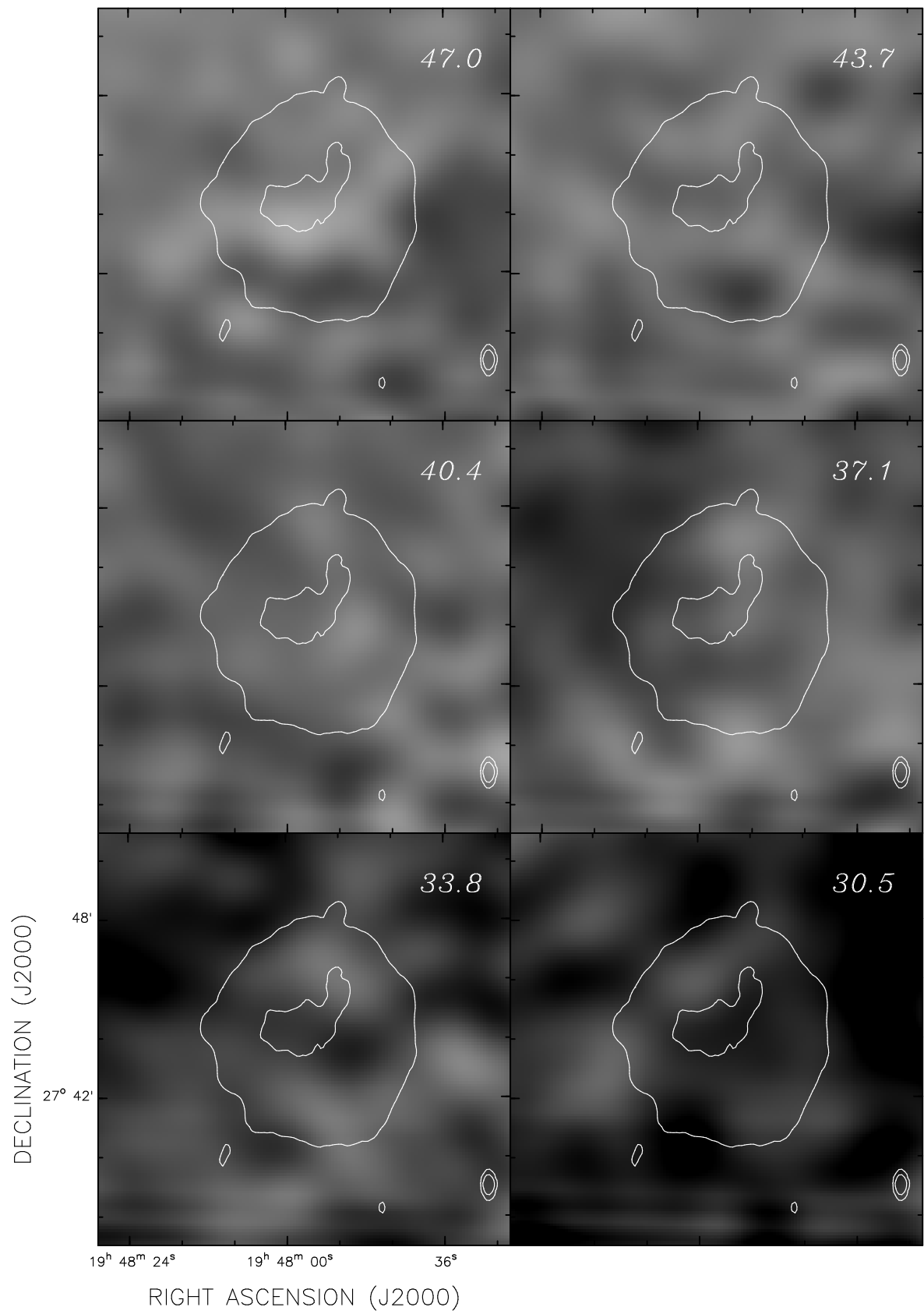
RIGHT ASCENSION (J2000)

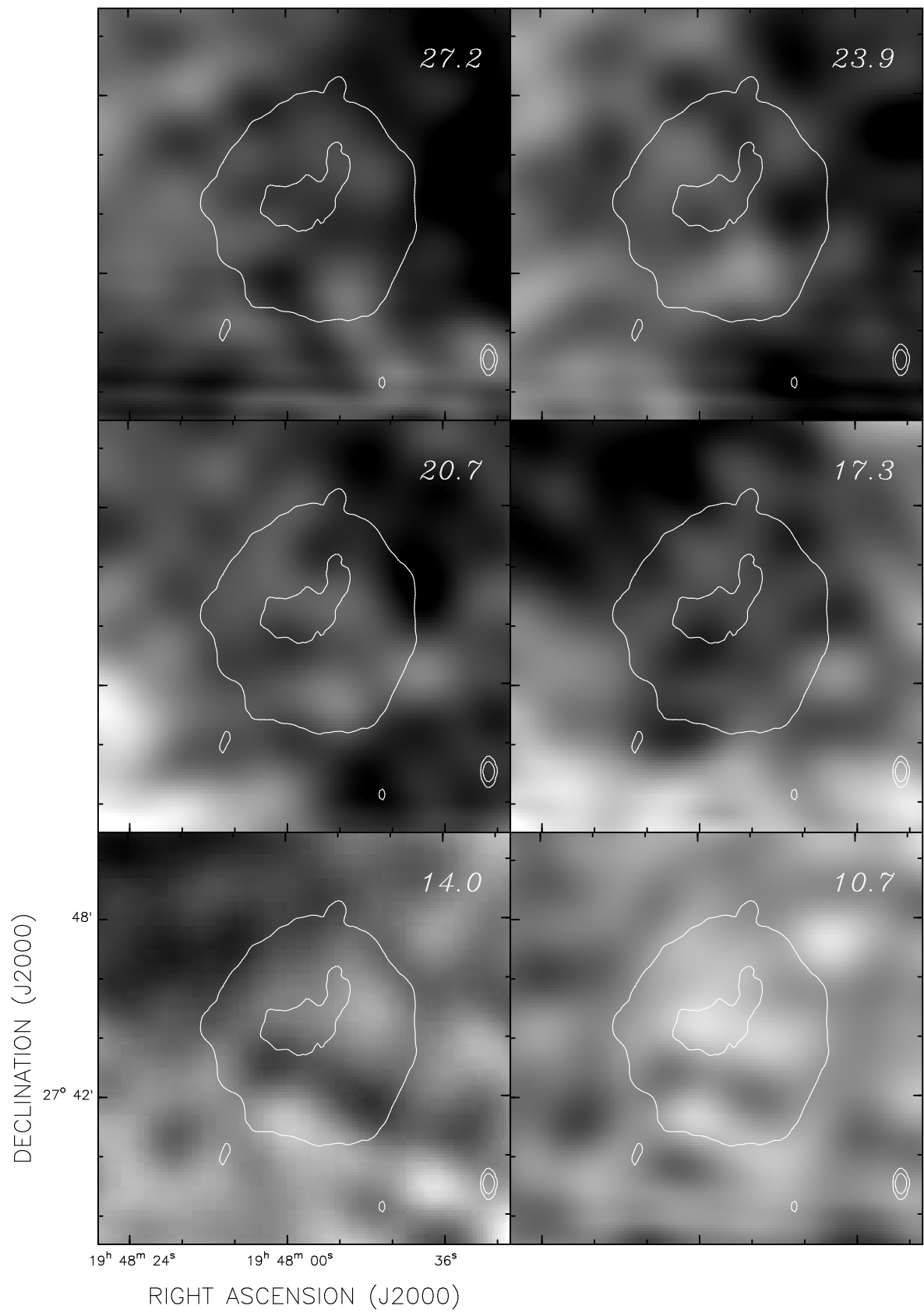


RIGHT ASCENSION (J2000)

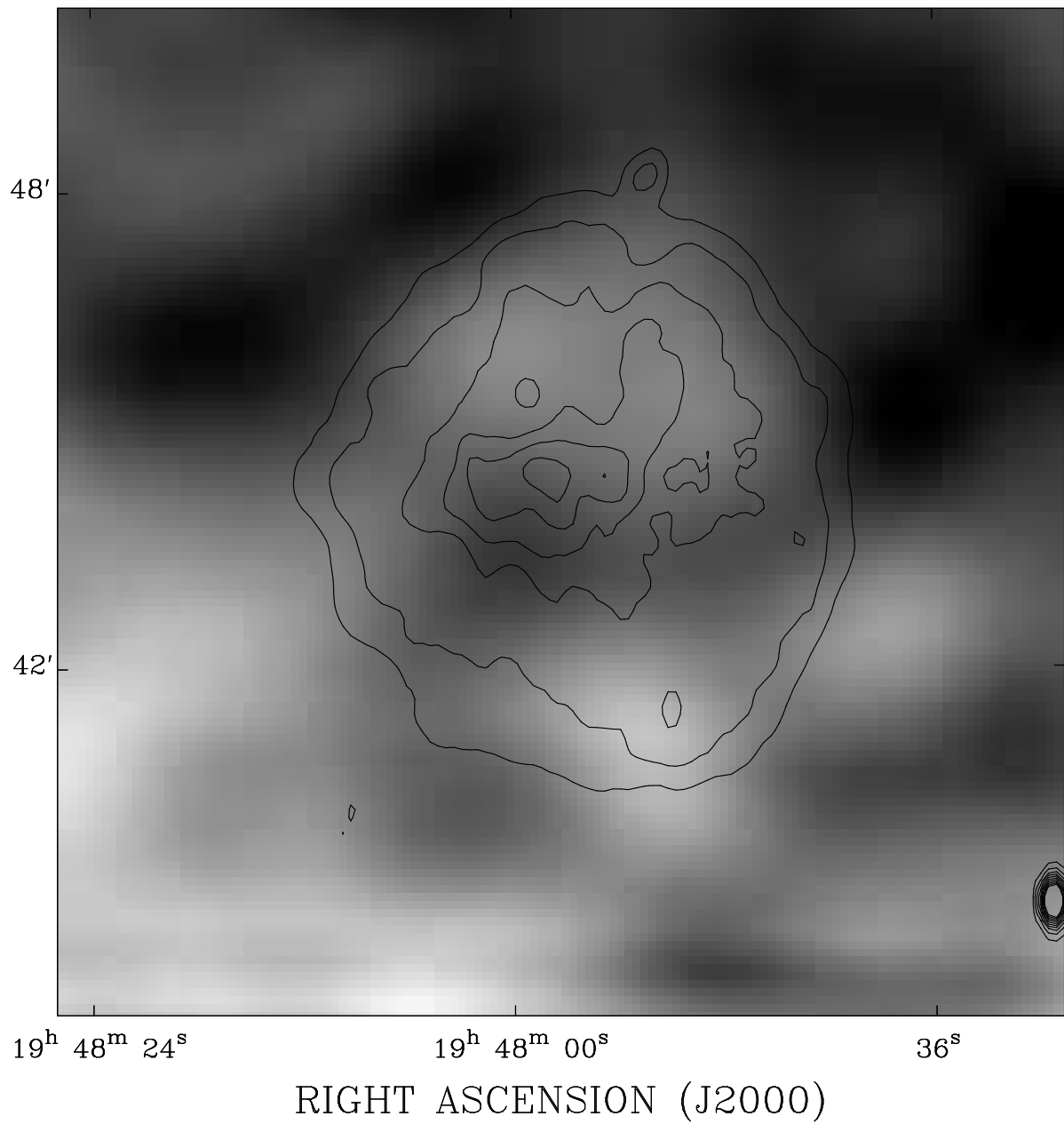


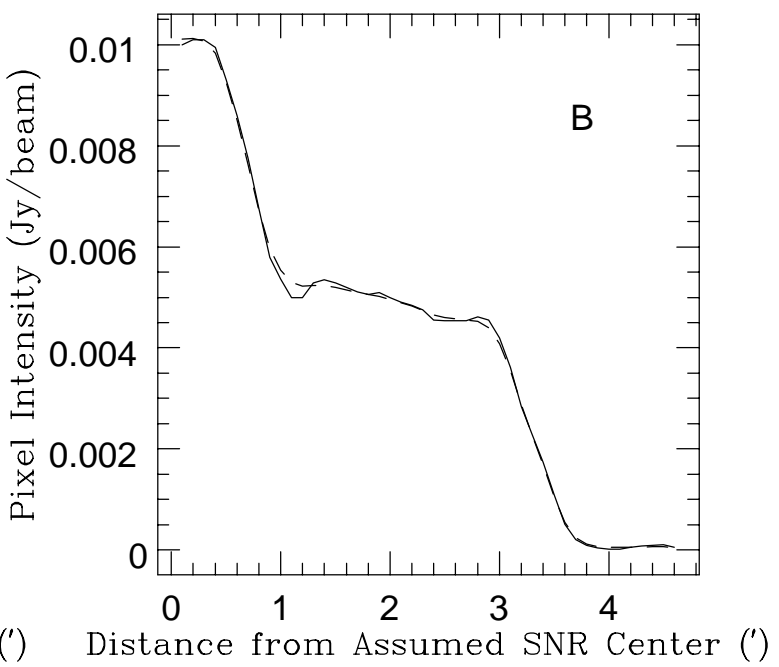
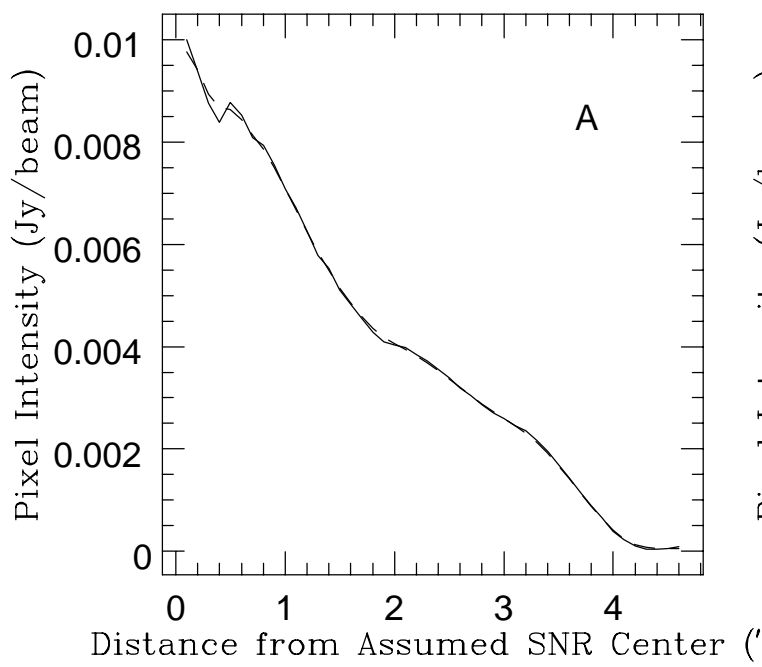
RIGHT ASCENSION (J2000)

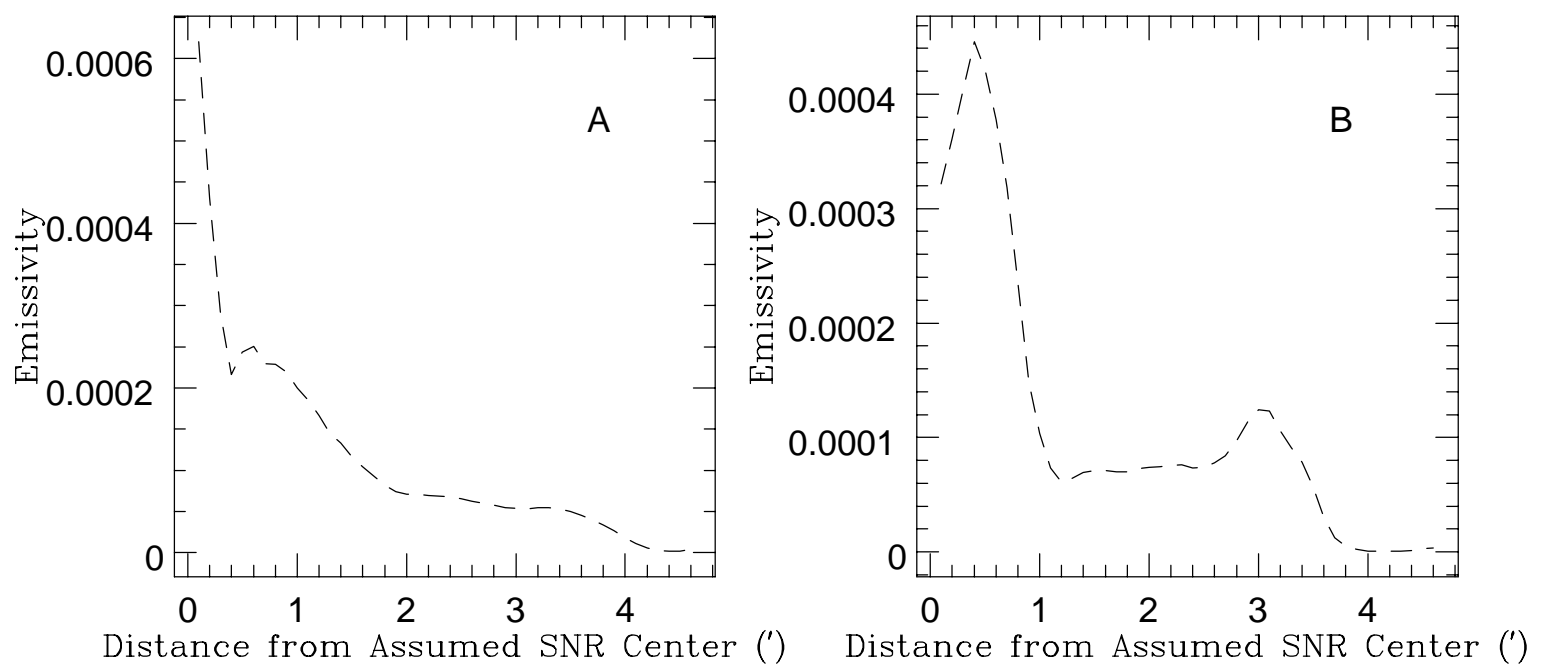


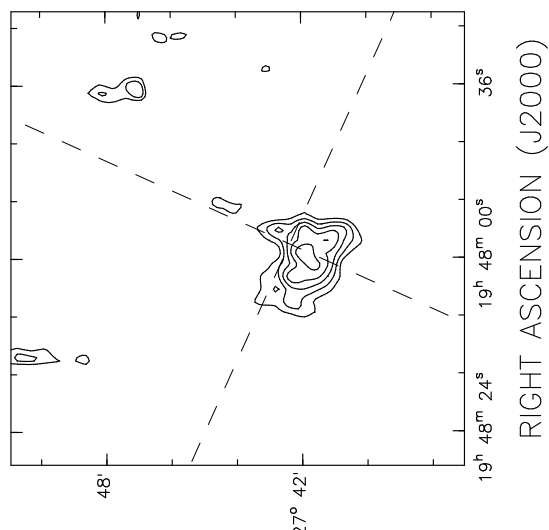


DECLINATION (J2000)



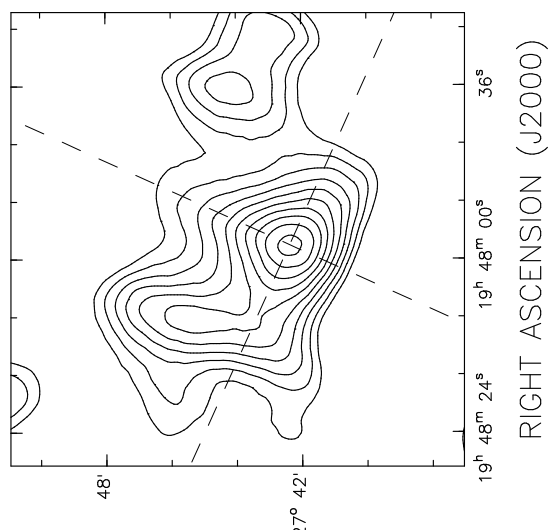






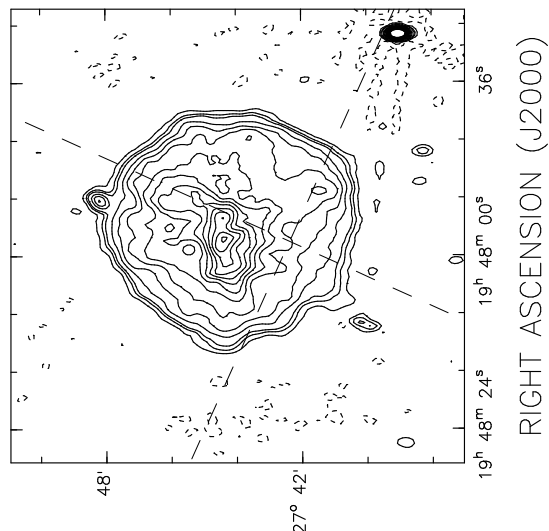
DECLINATION (J2000)

RIGHT ASCENSION (J2000)



DECLINATION (J2000)

RIGHT ASCENSION (J2000)



DECLINATION (J2000)

RIGHT ASCENSION (J2000)